Reduced-Order Analytical Model of Grid-Connected Solar Photovoltaic Systems for Low-Frequency Oscillation Analysis

Miao Zhang, *Student Member, IEEE,* Zhixin Miao, *Senior Member, IEEE,* Lingling Fan, *Senior Member, IEEE*

***Abstract*—Low-frequency oscillations have been observed in a real-world solar photovoltaic (PV) farm. The goal of this research is to build a simplified analytical model in the synchronous frame for large-signal simulation and small-signal analysis. The latter, e.g., eigenvalue analysis and participation factor analysis, can reveal influencing factors of the oscillations. Two simplified analytical models are proposed, ignoring PV dc-side dynamics (e.g., dc/dc boost converter control and maximum power point tracking), while preserving the grid-side converter (GSC) controls and electromagnetic dynamics of the grid interconnection. The first model assumes that the input power from PV's dc side is known and constant. The second model assumes that PV's dc side is represented by a constant dc voltage behind an impedance. The simplified models are compared with an electromagnetic transient (EMT) testbed with full details on time-domain simulation results, admittance frequency-domain responses, and eigenvalue-based stability analysis results. The second simplified model is found as capable of accurately predicting oscillation stability.**

***Index Terms*—Solar PV; weak grid; low-frequency oscillations; analytical model; admittance.**

I. Introduction

MORE and more inverter-based resources (IBRs) are integrated into power grids. In turn, the grid industry is facing operational challenges. One such challenge is instability due to IBRs integrated into weak grids [1]. In the real world, low-frequency oscillations at 4 Hz were observed in type-4 wind farms at Texas in 2011 [2]. These oscillations limit power exporting level of wind farms. As a mitigation approach, ERCOT installed two synchronous condensers at that region [3]. Consequently, the power exporting level is improved.

This dynamic phenomenon has been thoroughly analyzed recently, e.g., in [4]–[7]. The instability mechanism is summarized as follows. Due to grid-following control design, increasing power order of a voltage source converter (VSC) leads to the increase of d-axis current order, where d-axis aligns with the point of common coupling (PCC) voltage. An increase in the d-axis current leads to a decrease in the PCC voltage magnitude, which in turn results in a decrease in real power. Thus, an instability mechanism is introduced [4].

The particular dynamic phenomenon related to VSC in weak grids is termed as weak grid voltage stability by the grid industry [1]. Increased active power transfer level and weak grid interconnection may worsen stability [4], [5]. On the other hand, faster voltage control [7] and reactive power injection [3], [8] may relieve the stress on stability.

Since both type-4 wind farms and solar PVs employ grid-following VSC as the interface to power grids, it is plausible to think that solar PVs may also suffer low-frequency oscillations at weak grid conditions. This speculation is proved by the real-world observation: a utility-scale PV plant experienced 7 Hz oscillations in power measurement during transmission line outage [9].

Thus, the goal of this paper is to provide a computing efficient analytical model for a grid-connected solar PV farm with the capability of both large-signal simulation and small-signal analysis. The latter can reveal the influencing factors of low-frequency oscillations besides grid strength.

Nonlinear state-space models have been built for a grid-connected solar PV in the literature. A detailed PV system state space model, including GSC controls, dc/dc boost converter controls, has been built by B. Pal's group in [10], [11]. Reference [10] incorporates maximum power point tracking (MPPT) and irradiance-driven dynamics. In [11], a state-space model taking into account of all circuit dynamics is derived to examine system responses under irradiance fluctuation, grid faults and frequency distortion. On the other hand, the proposed models in [10], [11] assume that the PCC bus is connected to a stiff grid. Thus, the set of the models lacks the capability of stability analysis at weak grid interconnection where the PCC bus voltage is no longer a constant voltage source.

This paper will design a model suitable for weak grid operation. In addition, since the grid industry desires simplified models to represent solar PVs for system integration dynamic studies, a simplified model will be investigated.

According to stability analysis research conducted in 2010 for a 2 MW type-4 wind turbine grid integration system in [12], the low-frequency oscillations at about 10 Hz are related to the GSC control and the transmission line length. This research assumes a model of full details, including GSC controls, dc-link dynamics, machine side converter controls and permanent magnet synchronous machine dynamics. Based on this research, it is reasonable to preserve only GSC control dynamics and ac circuit dynamics in a simplified model while ignoring the rest. Indeed, the grid industry's practice on dynamic studies with IBR penetration, e.g., [13], ignores dc side dynamics to keep the overall model order from exploding.

Our prior work [5], [7], [14] on modeling and analysis of dynamics of type-4 wind farms for subsynchronous os-

M. Zhang, Z. Miao, and L. Fan are with the Department of Electrical Engineering, University of South Florida, Tampa, FL, 33620. e-mail: linglingfan@usf.edu

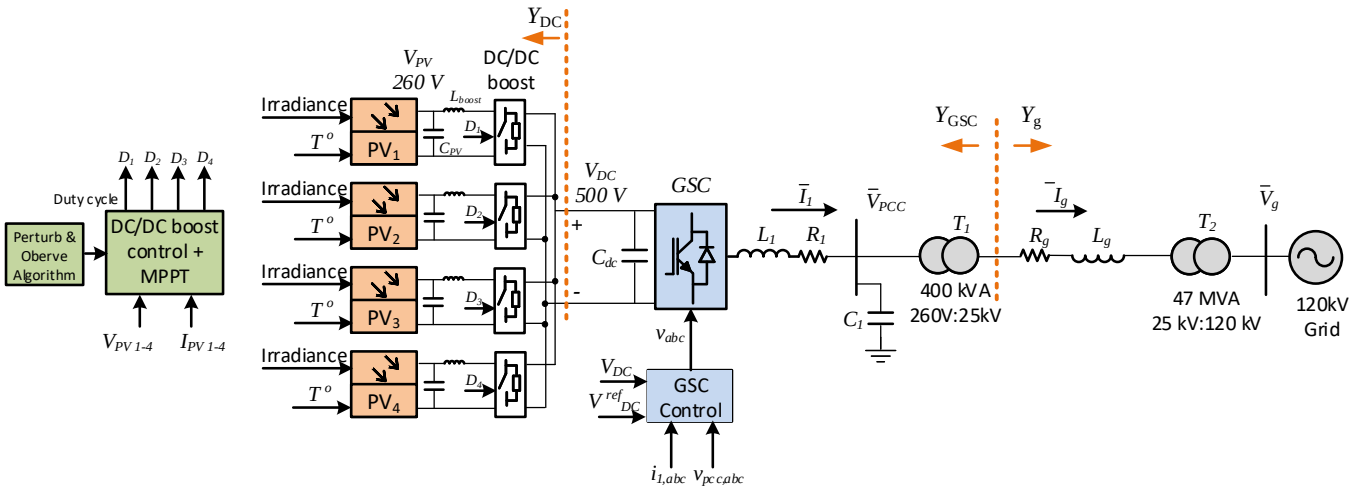

Fig. 1: EMT testbed: 400-kW grid-connected PV Farm. GSC assumes grid-following vector control relying on PLL. Y_{DC} and Y_{GSC} can be measured from the testbed.

cillations also suggests that analytical models representing dc side dynamics using a simplified model, e.g., constant input power, are suitable to predict stability issues related to weak grid operation. Comparison of time-domain simulation results against those from the models with full details has been conducted in [7], [14].

This paper makes an improvement on the models built in our prior work [5], [7], [14] by examining different dc side representations. While constant dc input power is assumed in [5], [7], [14], constant dc voltage assumption will be examined and compared with the constant input power assumption in this paper.

For validation, simplified models will be compared against an EMT testbed with full details, including all stages of PV system circuit dynamics and converter control dynamics. Dynamic simulation results, admittance frequency-domain responses, and eigenvalue analysis results of the simplified models will be compared with those of the EMT testbed.

The contribution of the paper is two-fold.

- A 15th-order nonlinear dq-frame model is built with the capability of large-signal simulation and small-signal analysis for a grid-connected solar PV farm. Specifically, the dc-side dynamics are represented by an equivalent circuit and its parameters can be found through the measured dc admittance. This model can accurately demonstrate low-frequency oscillations in a PV grid integration system. Small-signal analysis based on the model pinpoints influencing factors of the oscillations.

  As a comparison, though many research papers in the literature also have state-space models designed for grid-following converters, e.g., [15], [16], those models are linear models suitable for small-signal analysis only.
- This paper provides a thorough model validation approach. The proposed simplified models are compared with the EMT testbed with full details on not only time-domain simulation results, but also frequency-domain responses of solar PV admittances. In addition, stability analysis results are compared using system eigenvalues. For the analytical models in the synchronous frame, linear models can be found through numerical perturbation. With linear models, eigenvalues can be computed. For the EMT testbed where three-phase instantaneous voltages and currents are state variables, measurement data-based admittance characterization is adopted to obtain admittance. Not only the conventional sinusoidal harmonic injection or frequency scan is employed but also time-domain step response-based method is employed. With the PV system admittance available and the grid interconnection admittance derived, s-domain admittance-based eigenvalue analysis proposed in 1990s in [17] is utilized for stability analysis. This method is found to lead to accurate stability analysis compared to Bode plot stability criterion [18].

The remainder of the paper is organized as follows. Section II first introduces the 400-kW PV farm grid integration EMT testbed. Low-frequency oscillations are demonstrated. The admittance of the PV farm is also characterized. s-domain admittance-based eigenvalue analysis is then conducted to find stability limit. Section III describes the simplified models and presents the comparison results on dynamic simulation, admittance, and eigenvalue analysis. Section IV presents the participation factor analysis of the selected simplified model. The paper is concluded in Section V.

II. Detailed EMT Testbed

The testbed is developed based on the 400-kW grid-connected PV farm demo in MATLAB/SimPowerSystems [19]. A 400 kW 260 V PV system is integrated into a 120 kV grid through a step transformer, 25 kV line, and another step-up transformer.

The transmission topology and converter controls have been tuned for this research. The topology diagram is shown in Fig. 1. The GSC assumes PCC voltage oriented grid-following vector control and it regulates dc-link voltage and PCC voltage. The phase-locked loop (PLL) has three-phase PCC voltage as the input and outputs the PCC voltage angle. The PLL is also

used to synchronize the converter to the grid. Details of the converter control can refer to Fig. 9. The PV farm consists of four PV arrays connected in parallel. Each array has a capability of 100 kW at 1000 W/m^2 sun irradiance.

The PV voltage (V_{PV}) is the PV array output voltage, or the input voltage to a dc/dc boost converter. The dc/dc boost converter control realizes MPPT, which adopts "perturb and observe" technique. The dc/dc booster's output voltage is at 500 V level. This 500 V dc voltage is converted to a three-phase 260 V ac voltage by a VSC. A shunt capacitor (C_1) is connected at the PCC bus to provide reactive power. Two transformers (T_1, T_2) step the 260 V ac voltage to 25 kV and 120 kV, respectively. The system parameters are given in Table I.

TABLE I: PV System Parameters

Description	Parameters	Value
Power base	S_{base}	400 kW
Power level	P_{PCC}	0.935 pu
System frequency	f_{base}	60 Hz
Converter filter	R_1	0.15/50 pu
	X_1	0.15 pu
Shunt capacitor	C_1	0.25 pu
DC-link capacitor	C_{dc}	0.054 F
Transmission system	R_g	$0.1X_g$
Inner loop	K_{pi}, K_{ii}	0.3, 5
DC-link control loop	K_{pp}, K_{ip}	1, 100
V_{ac} control loop	K_{pv}, K_{iv}	1, 100
Q control loop	K_{pq}, K_{iq}	1, 100
PLL	$K_{p,\text{PLL}}$, $K_{i,\text{PLL}}$	60, 1400
Feedforward filter	T_{VF}	0.001

The steady-state limits of the system, denoted by the aggregated transmission system (from the PCC bus to the 120 kV grid) reactance X_g, can be found by load flow. The transmission system resistance is assumed to be 10% of the reactance. Table II presents the two limits: 1.16 pu when the GSC is in PCC voltage control mode and 0.74 pu when the GSC is in reactive power control mode. In both cases, the real power delivery from the GSC to the PCC bus is kept at 0.935 pu.

TABLE II: Steady-State Limits

Control mode	$P_{\text{PCC}} = 0.935$ pu
PCC voltage control: $V_{\text{PCC}} = 1.0$ pu	$X_g = 1.16$ pu
Reactive power control: $Q_{\text{PCC}} = 0$ pu	$X_g = 0.74$ pu

Low-frequency oscillations at $7 \sim 8$ Hz can be observed when the transmission line impedance X_g is 1.0 pu. The GSC assumes dc-link voltage control mode in the d-axis and PCC voltage control mode in the q-axis. Fig. 2 (a) and (b) present the system dynamic responses when the PCC voltage control's order (V^*_{PCC}) steps from 1.0 pu to 0.99 pu at $t = 4$ s.

It can be clearly seen that the system is at the marginal stability condition. Fig. 2 (a) shows that 7 Hz oscillations appear in PV's 500 V dc-link voltage, dc-side current and power. Fig. 2 (b) shows that 7 Hz oscillations appear in PV's ac side dq-frame current and voltage as well as real power and reactive power measured at the PCC bus.

Thus, it can be found that oscillations reduce the limit of operation from $X_g = 1.16$ pu to $X_g = 1.0$ pu.

A. Solar PV admittance characterization

Harmonic injection method or frequency scan method is the most popular method applied for admittance or impedance characterization [20]–[23]. A measurement testbed is first built with a PV farm connected to a voltage source at the measurement point. The measurement point has been notated as the dotted line after the 260 V/25 kV transformer in Fig. 1. First, the PV farm's operating condition, defined by the measured real power and reactive power to the PCC bus from the converter and the PCC bus voltage magnitude, is set to be the same as the EMT testbed. The dq-frame admittance characterization relies on d-axis voltage perturbation and q-axis voltage perturbation.

For harmonic injection method or frequency scan, the q-axis voltage is kept intact, sinusoidal injection at a frequency ω_p with a known magnitude is added on top of the d-axis voltage. The dq-axis currents from the converter are measured and the harmonic components at ω_p frequency are found via fast Fourier transform (FFT). From this set of experiment, three phasors are found $\Delta v_d(j\omega_p)$, $\Delta i_d(j\omega_p)$, and $\Delta i_q(j\omega_p)$. Thus, the admittance matrix's dd and qd components at ω_p frequency can be found as

$$Y_{dd}(j\omega_p) = -\frac{\Delta i_d(j\omega_p)}{\Delta v_d(j\omega_p)},\ Y_{qd}(j\omega_p) = -\frac{\Delta i_q(j\omega_p)}{\Delta v_d(j\omega_p)}.$$

Similarly, the dq and qq components can be found by v_q perturbation. To obtain the admittance measurement for a span of frequency range, hundreds of experiments need to be carried out. Fig. 4a presents the Bode plot of the measured admittance obtained by frequency scan.

An alternative method for admittance characterization is to use time-domain data. When the time-domain data of the input and output channels are obtained, well-known system identification algorithms, such as numerical algorithm for subspace state space system Identification (N4SID) [24], Multivariable Output-Error State Space (MOESP) [25], and Eigensystems Realization Algorithm (ERA) [26], can be employed. Among them, ERA has been applied in power systems to identify reduced-order input/output linear models for power system stabilizer design and FACTs controller design [27]. An in-house toolbox relying on ERA algorithm to estimate time-domain measurement's transfer function has been designed for PV farm admittance estimation in this research. Details of ERA can be found in a tutorial paper from the authors' research group [28].

The perturbation is designed as a step change in d-axis or q-axis voltage. Each small-signal perturbation generates two time-domain responses: dq-axis currents exporting from the PV farm to the voltage source: $i_d^{(k)}(t)$ and $i_q^{(k)}(t)$, where $k = 1, 2$ notates the index of each experiment. With the transfer functions of $i_d^{(k)}(s)$ and $i_q^{(k)}(s)$ being identified, the admittance model can be found as:

$$Y_{\text{GSC}} = -\begin{bmatrix} \frac{i_d^{(1)}(s)}{v_d^{(1)}(s)} & \frac{i_d^{(2)}(s)}{v_d^{(2)}(s)} \\ \frac{i_q^{(1)}(s)}{v_d^{(1)}(s)} & \frac{i_q^{(2)}(s)}{v_q^{(2)}(s)} \end{bmatrix} = -\frac{s}{p}\begin{bmatrix} i_d^{(1)}(s) & i_d^{(2)}(s) \\ i_q^{(1)}(s) & i_q^{(2)}(s) \end{bmatrix} \quad (1)$$

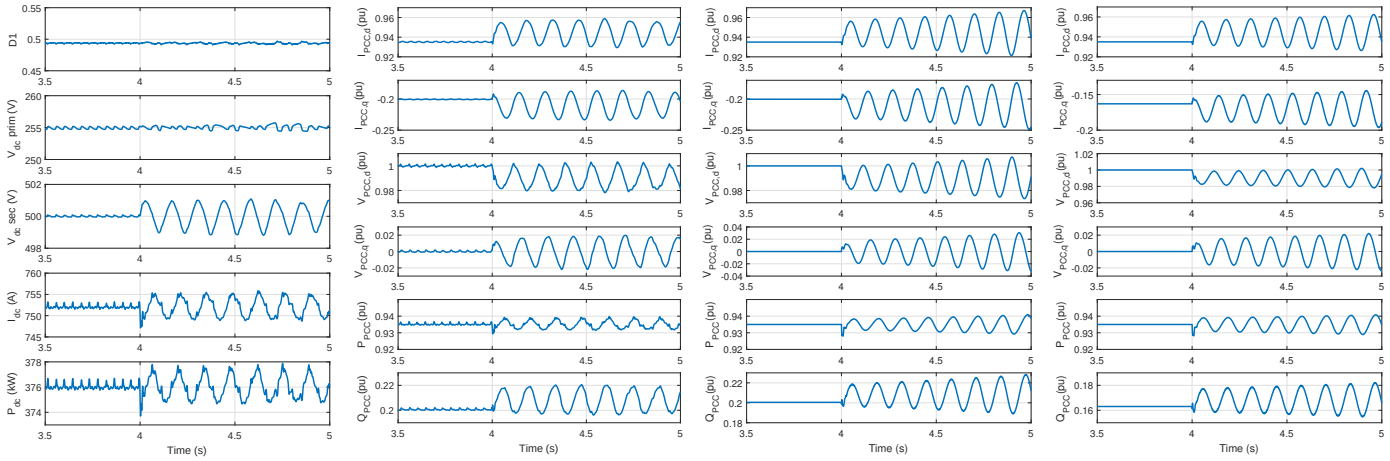

Fig. 2: Dynamic responses of the EMT testbed with full details (a)(b), and two simplified models (c)(d). V^*_{PCC} steps from 1.0 to 0.99 at $t = 4$ s. (a) Detailed testbed: dc side variables (duty cycle of the dc/dc boost converter, PV side voltage, boost converter output voltage, dc side current and dc side power); (b) Detailed testbed: ac side variables (dq-axis GSC current to the PCC bus, dq-axis PCC bus voltage, and real and reactive power to PCC bus), $X_g = 1.0$ pu; (c) Constant dc voltage simplified model: ac side variables (dq-axis GSC current to the PCC bus, dq-axis PCC bus voltage, and real and reactive power to PCC bus), $X_g = 1.0$ pu; (d) Constant input power simplified model: ac side variables (dq-axis GSC current to the PCC bus, dq-axis PCC bus voltage, and real and reactive power to PCC bus), $X_g = 0.96$ pu.

where p is the size of perturbation and $v_d^{(1)}(s) = v_q^{(2)}(s) = p/s$. The negative sign is due to the current direction as flowing out of the PV.

The measurement point is close to the PCC bus. A small impedance (e.g., $0.01 + j0.1$ pu) is usually inserted between the PCC bus and the measurement point.

First, 2% step change is applied to the d-axis voltage and $i_{g,d}^{(1)}$, $i_{g,q}^{(1)}$ are measured. Next, 2% step change is applied to the q-axis voltage and $i_{g,d}^{(2)}$, $i_{g,q}^{(2)}$ are measured.

$i_{g,d}^{(1)}$, $i_{g,q}^{(1)}$, $i_{g,d}^{(2)}$, $i_{g,q}^{(2)}$ are fed into the toolbox for estimation. The estimated currents by the toolbox are plotted along with the original measured data in Fig. 3. The estimated system order is defined as 18. Additionally, the sampling period is 0.25 second with 2 kHz sampling rate. The Bode plots of the estimated admittance are shown as the solid lines in Fig. 4a.

Remarks: It can be seen that the time-domain data based estimation and frequency scan method lead to very similar admittance. In addition, frequency scan leads to admittance measurements at those perturbed frequencies while the time-domain data based method leads to an analytical model in s-domain. The latter can be directly used for eigenvalue analysis.

B. s-domain admittance-based eigenvalue analysis

In the power grid industry, small-signal analysis is usually conducted by examining the eigenvalues of linear models, which are obtained from nonlinear dq-frame models through numerical perturbation [29]. On the other hand, a system can be divided into subsystems. With each subsystem viewed as an admittance, the entire system may be viewed as a circuit consisting of admittances. Stability analysis can be carried out using the network admittance. The two approaches lead to the same eigenvalues with benchmarking results presented in [30].

The system in Fig. 1 is viewed at the measuring point with two shunt admittances: Y_{GSC} and Y_g, where Y_{GSC} is the admittance of the subsystem at the left of the measurement point and Y_g is the Norton equivalent admittance of the grid interconnection at the right of the measurement point.

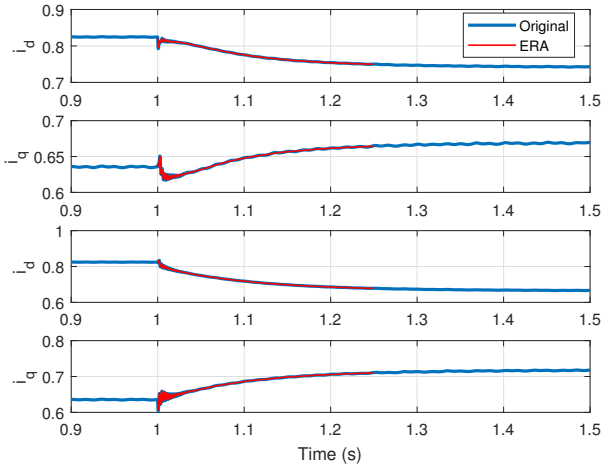

Fig. 3: Original measurement and the reconstructed signal using estimated eigenvalues.

Applying circuit analysis, it can be found the relationship between the injected small current at the measuring point and the voltage of the measuring point as follows.

$$\begin{bmatrix}\Delta i_{d,\text{inj}}\\ \Delta i_{q,\text{inj}}\end{bmatrix} = (Y_{\text{GSC}} + Y_g)\begin{bmatrix}\Delta v_d\\ \Delta v_q\end{bmatrix} \tag{2}$$

If (2) is viewed as an input/output system, then the PCC voltage is the output (notated as y) and the injected current is the input (notated as u). Hence, the transfer function matrix notated as $G(s)$ from u to y is:

$$G(s) = \underbrace{(Y_{\text{GSC}} + Y_g)}_{Y}{}^{-1} \tag{3}$$

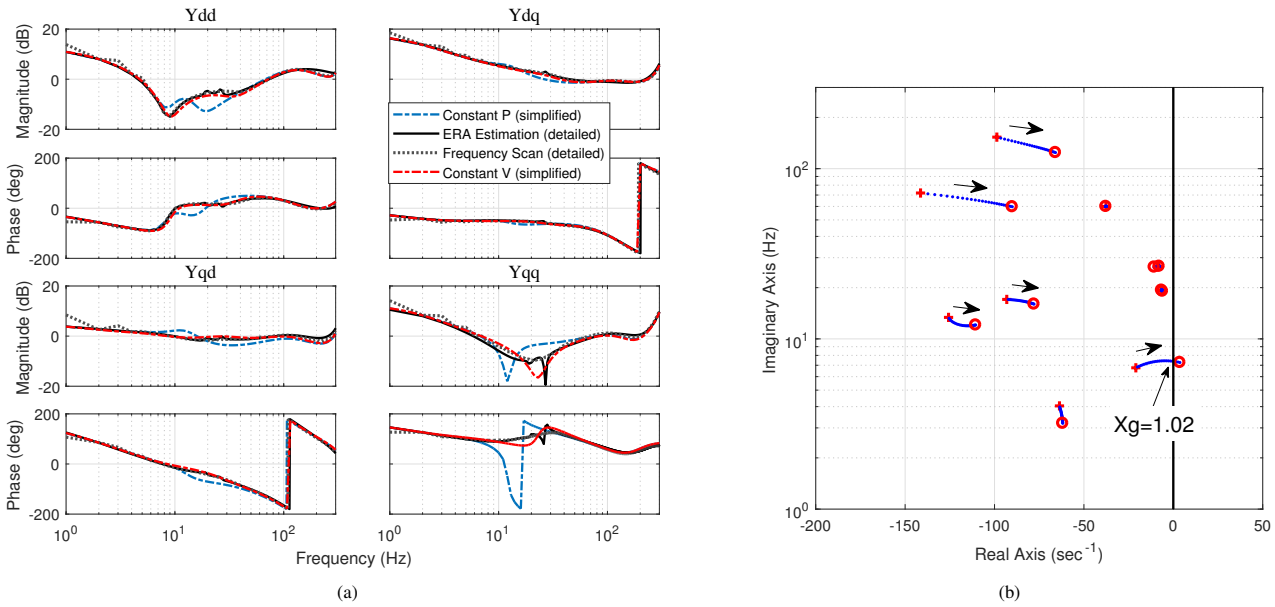

(a) (b)

Fig. 4: (a) Bode plots of the admittance models. Dash-dot lines: simplified models. Solid lines: ERA estimation from detailed model. Dotted lines: frequency scanning from detailed model. (b) Eigenvalues of the detailed model where X_g varies from 0.5 to 1.1 pu.

where

$$Y_g = \begin{bmatrix} R_g + sL_g & -\omega_0 L_g \\ \omega_0 L_g & R_g + sL_g \end{bmatrix}^{-1},$$

and ω_0 is the nominal frequency 377 rad/s.

Poles of $G(s)$ are the eigenvalues of the system. In turn, roots of $\det(Y)$ or the zeros of the s-domain admittance matrix Y are the eigenvalues of the system.The eigenvalues of whole system can be found as the zeros of $(Y_{\text{GSC}} + Y_g)$. The aforementioned eigenvalue analysis tool was proposed in [17] by Semlyen and termed as s-domain admittance based eigenvalue analysis. Most recently, this approach has been adopted in [18], [31] for power grids with IBR penetrations.

By varying grid side admittance, the whole system eigenvalue trajectory can be found and presented in Fig. 4b. The marginal condition $X_g = 1.02$ pu is accurately predicted and corroborates with the simulation results in Fig. 2(a)(b).

III. Simplified Analytical Models

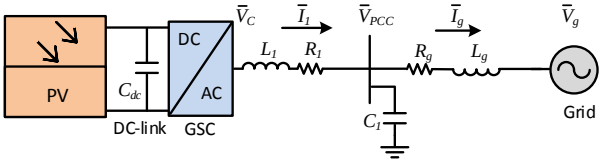

Fig. 5: Per unit circuit diagram of a grid connected PV farm.

The simplified nonlinear analytical models are based on a per unit circuit diagram shown in Fig. 5. Resistances and inductances of the transformers and the transmission line are aggregated into R_g and L_g, respectively.

A. DC side representation

The dc side dynamic has a coupling effect on ac side [32]. Thus, it is obvious that different dc side representations will have affect on the admittance viewed from the ac side.

Besides constant input power assumption adopted in [7], constant dc voltage assumption is examined. The circuit representations are presented in Fig. 6. Fig. 6(a) presents the constant input power assumption. In the case of constant input power, the dc side is assumed to be a controllable current source with its power P_{pv} given.

Fig. 6(b) is the constant dc voltage representation. The dc side is treated as an equivalent circuit: a constant dc voltage source behind an RLC circuit.

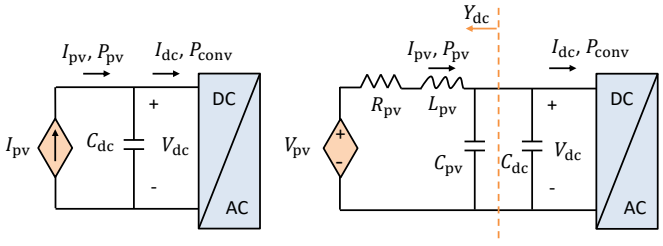

Fig. 6: Simplified models to represent the dc-side dynamics. (a) Constant P_{pv} model; (b) Constant V_{pv} model.

Constant power model: The input power from PV dc side to the dc-link is given as P_{pv}. The dc-link capacitor dynamic can be expressed by (4).

$$\frac{C_{\text{dc}}}{2}\frac{dV_{\text{dc}}^2}{dt} = P_{\text{pv}} - P_{\text{conv}} \tag{4}$$

where P_{pv} is a constant value, and P_{conv} is computed by the ac side variables (converter output voltage v_{dq} and current i_{1dq}) and $P_{\text{conv}} = v_d i_{1d} + v_q i_{1q}$ in per unit. The block diagram is presented in Fig. 7 (a). The output V_{dc}^2 in per unit will be fed into VSC control in the analytical model block diagram in Fig. 9.

Constant voltage model: The shunt capacitor $C_{\rm pv}$ can be ignored if $C_{\rm pv} \ll C_{\rm dc}$. The dc-link capacitor dynamics and the inductor dynamics can be expressed in (5) and (6). Fig. 7 (b) presents the block diagram for the constant dc voltage source model.

$$\frac{C_{\rm dc}}{2}\frac{dV_{\rm dc}^2}{dt} = I_{\rm pv}V_{\rm dc} - P_{\rm conv} \tag{5}$$

$$L_{\rm pv}\frac{dI_{\rm pv}}{dt} = V_{\rm pv} - V_{\rm dc} - I_{\rm pv}R_{\rm pv} \tag{6}$$

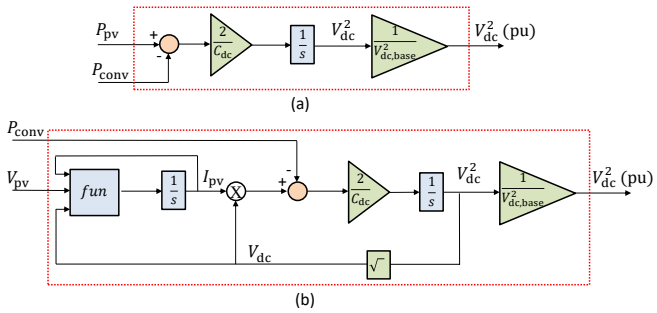

Fig. 7: DC-side dynamics modeling. (a) Constant $P_{\rm pv}$; (b) Constant $V_{\rm pv}$.

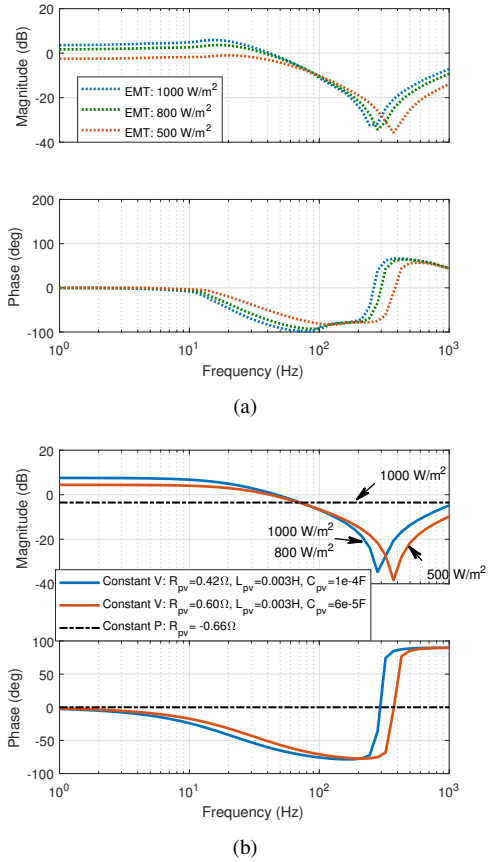

Fig. 8: The DC side admittance viewed from the dc-link bus. (a) The measured frequency responses under different irradiance conditions from the EMT testbed. (b) Simplified model frequency responses under different assumptions.

To determine $R_{\rm pv}$ and $L_{\rm pv}$, the admittance viewed at the dc-link bus of the EMT testbed will be measured via the sinusoidal harmonic injection. The dc side measurement point ($Y_{\rm DC}$) is marked in Fig. 1. The frequency responses are shown by Bode plots in Fig. 8 (a) with the three dotted lines representing three different irradiance conditions.

$R_{\rm pv}$, $L_{\rm pv}$, and $C_{\rm pv}$ are properly selected to fit the frequency responses of the measured admittance. In Fig. 8 (b), the constant voltage with $R_{\rm pv} = 0.42\ \Omega$, $L_{\rm pv} = 0.003$ H, $C_{\rm pv} = 1e^{-4}$ F is adopted to represent the dc side system when the irradiance is 1000 W/m^2 or 800 W/m^2, since those two scenarios have very similar frequency responses. The constant voltage with $R_{\rm pv} = 0.6\Omega$, $L_{\rm pv} = 0.003$ H, and $C_{\rm pv} = 6e^{-5}$ F is adopted to represent the dc side system when the irradiance is 500 W/m^2. They are listed in Table III. Notice that $C_{\rm pv}$ is very small comparing to C_{dc} (0.0543 F), so $C_{\rm pv}$ can be ignored in the simplified model.

TABLE III: The corresponding $R_{\rm pv}$, $L_{\rm pv}$, and $C_{\rm pv}$ regarding different irradiance conditions

Irradiance (detailed)	Constant voltage $R_{\rm pv}$, $L_{\rm pv}$ (simplified)
1000 W/m^2	$R_{\rm pv} = 0.42\ \Omega$, $L_{\rm pv} = 0.003$ H, $C_{\rm pv} = 1e^{-4}$ F
800 W/m^2	$R_{\rm pv} = 0.42\ \Omega$, $L_{\rm pv} = 0.003$ H, $C_{\rm pv} = 1e^{-4}$ F
500 W/m^2	$R_{\rm pv} = 0.60\ \Omega$, $L_{\rm pv} = 0.003$ H, $C_{\rm pv} = 6e^{-5}$ F

As a comparison, the Bode plot of constant power assumption is presented as the black dash-dot line in Fig. 8 (b). The dc side can be viewed as a resistor under the constant dc power source assumption:

$$\Delta P_{\rm pv} = V_{\rm dc}\Delta I_{\rm dc} + I_{\rm dc}\Delta V_{\rm dc} = 0$$

$$R_{\rm pv} = -\frac{\Delta V_{\rm dc}}{\Delta I_{\rm dc}} = \frac{V_{\rm dc}}{I_{\rm dc}},$$

where $I_{\rm dc}$ is the dc current when the irradiance is 1000 W/m^2. Significant difference exists between this admittance and the measured admittance.

B. Grid-connected VSC representation

Modeling of grid-connected VSC has been addressed in the authors prior work, e.g., [5]–[7]. Brief explanation of the modeling assumption is given in the following.

The block diagram of the dq-frame based model is shown in Fig. 9. The two simplified models have orders of 14 (constant input power assumption) and 15 (constant dc voltage assumption).

This dynamic model consists of a 6-order grid dynamic block where two inductors and one shunt capacitor dynamics are considered, a 2-order synchronous reference frame-based PLL, a 4-order vector control, a 1-order voltage feedforward low-pass filter and a 1-order (for constant power assumption) or 2-order (for constant dc voltage assumption) dc side dynamics.

The grid-connected converter model is based on two dq reference frames: converter-based frame (denoted as superscript c) for vector control and grid frame (denoted as superscript g) for grid dynamics. At steady-state, the d-axis of the converter

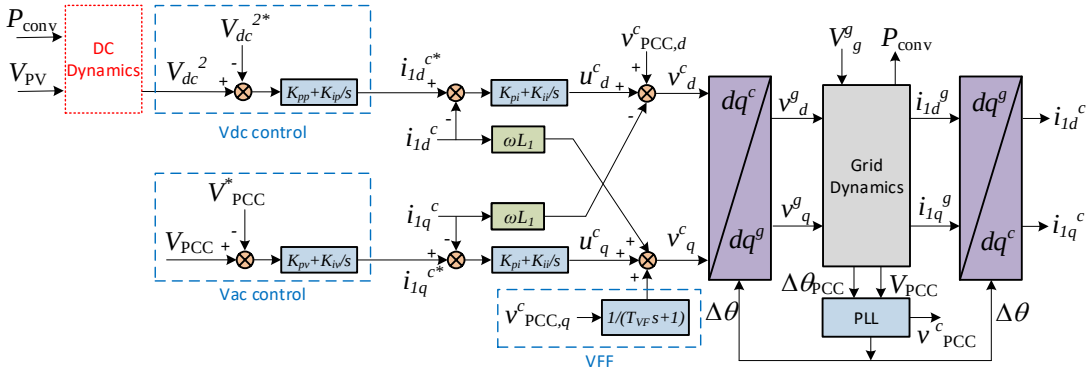

Fig. 9: Block diagram of the grid-connected VSC dynamic model. The block DC dynamics is represented in Fig. 7.

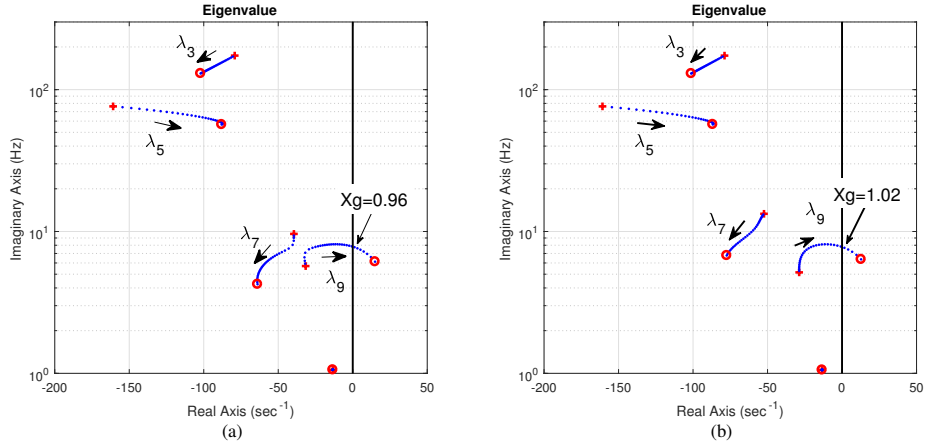

Fig. 10: Eigenvalues of simplified models where X_g varies form 0.5 to 1.10 pu, with each step 0.02 pu. (a) constant input power; (b) constant dc voltage.

frame aligns with the PCC voltage space vector, while the d-axis of the grid frame aligns with the grid voltage space vector. The converter frame is based on the PLL output angle. Thus, the converter frame leads the grid frame by the PLL output angle $\Delta\theta$.

More details on dq-frame based dynamic modeling, PLL details for a grid-connected VSC in real power control and ac voltage control mode can be found in the authors' prior work [5]–[7].

The converter control is based on the converter frame. In the outer loop of the converter control, d-axis is for dc-link voltage regulation while the q-axis is for ac voltage or reactive power regulation. The dc-link voltage control generates d-axis current reference i_{1d}^{c*} while the voltage or var control generates q-axis current reference i_{1q}^{c*}. The inner current controls have faster bandwidth to track the current orders. Current decoupling feedforward [33] has been adopted in the inner control. The q-axis voltage feedforward $v_{\mathrm{PCC},q}^{c}$ with a voltage feedforward filter (VFF) has been added in VSC control to enhance the system stability.

The converter control leads to controllable dq-axis converter output voltage in the converter frame. In the dynamic model block diagram in Fig. 9, the converter is treated as controllable voltage source for the circuit. This voltage source is converted into a voltage source in the grid frame and fed into the grid dynamics block. Outputs of the grid dynamics block are dq-axis converter current and PCC voltage in the grid frame. In turn, the PCC voltage phase angle $\Delta\theta_{\mathrm{PCC}}$ are also exported to feed into the PLL block to generate the PLL angle $\Delta\theta$. $\Delta\theta$ is used as the input for frame conversion. Real and reactive power of converter output may also be calibrated by the grid dynamics block.

Remarks: Thus, the entire analytical model is built in dq-frames. The model is a nonlinear model since no assumption of linearization has been made. For example, power expressions are nonlinear to voltage and currents; frame conversion uses sine and cosine of the PLL output angle. At balanced operating conditions, this model has state variables as constants at equilibrium points. Numerical perturbation can be implemented to easily extract the linearized models for small-signal analysis.

C. Comparison with the EMT testbed

Fig. 10 presents the loci of eigenvalues with a varying X_g. It can be seen that the dominant 7.8 Hz mode moves towards the right half plane (RHP) when X_g increases or the grid becomes weaker. Thus, both of the two simplified models can demonstrate low-frequency oscillations due to weak grid interconnection. The constant input power model identifies $X_g = 0.96$ pu as the marginal condition, while the constant dc voltage model identifies $X_g = 1.02$ pu as the marginal

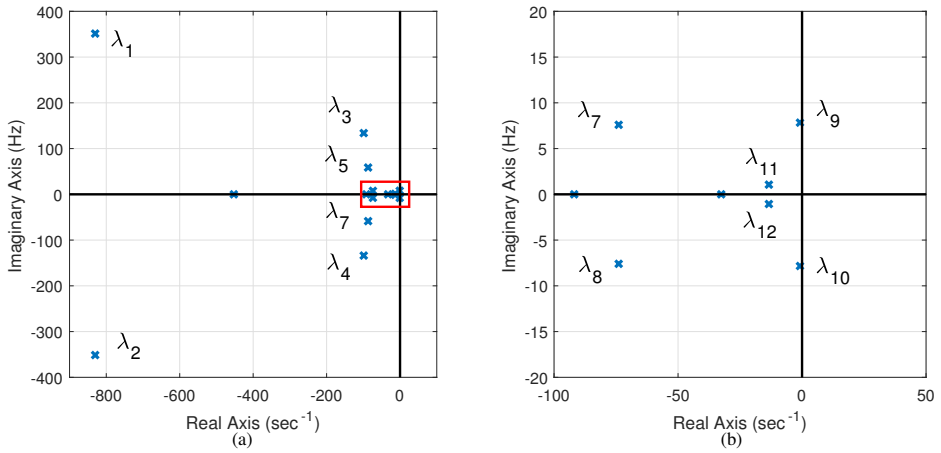

Fig. 11: Constant dc voltage model's eigenvalues when $X_g = 1.0$ pu. (b) is the zoom-in of the low-frequency modes in (a).

condition. Note that the detailed model indicates that 1.02 pu is the marginal condition. The prediction of the constant dc voltage model is the same as that from the s-domain admittance-based eigenvalue analysis in Fig. 4b.

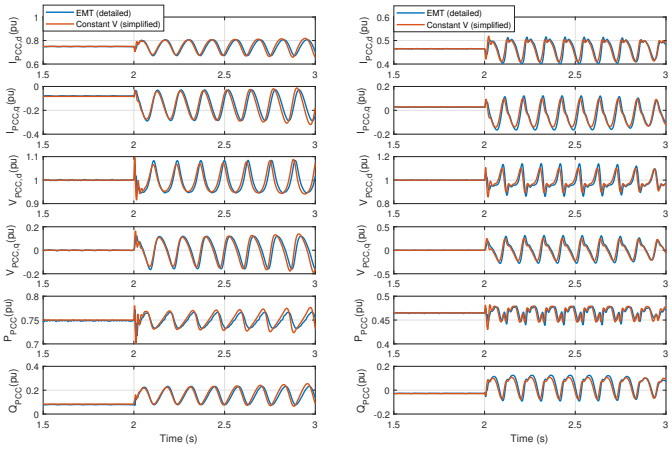

Fig. 12: Time-domain dynamic responses of line tripping in the EMT testbed and the constant voltage model. (a) X_g steps from 1.20 to 1.30 p.u. Blue line: irradiance at 800 W/m^2 in the EMT testbed. Red line: $R_{\text{pv}} = 0.42\,\Omega$, $L_{\text{pv}} = 0.003$ H in the simplified model. (b) X_g steps from 2.00 to 2.19 p.u. Blue line: irradiance at 500 W/m^2 in the EMT testbed. Red line: $R_{\text{pv}} = 0.6\Omega$, $L_{\text{pv}} = 0.003$ H in the simplified model.

Dynamic simulation with irradiance at 1000 W/m^2 is carried out using the simplified models. Fig. 2 (c)(d) present the constant dc voltage model 's and constant input power model's dynamic responses at the corresponding marginal conditions (X_g at 1.00 pu and 0.96 pu, respectively). The dynamic event is a small change in the PCC voltage order. It can be seen that 7 $\sim$ 8 Hz oscillations appear in both models. Furthermore, another two irradiance conditions are examined using constant voltage simplified model and the simulation results line tripping events are presented in Fig. 12.

Finally, frequency-domain responses of the two simplified models and EMT detailed model are compared. The Bode plots are presented in Fig. 4a. It can be seen that the two simplified models and the detailed model have comparable frequency-domain responses, especially in the low-frequency range. Among the two simplified models, the constant dc voltage model is more similar to the EMT detailed model. It is found that the qq component of the admittance (Y_{qq}) shows notable difference in magnitude and phase angle near 10 Hz for the constant input power model and the detailed EMT model. That is due to the dc side frequency responses mismatching shown in Fig. 8 (b).

Remarks: Based on comparison of time-domain simulation results, eigenvalue-based stability analysis results, and frequency-domain responses of admittances, it is found that the 15th-order constant dc voltage model is more accurate for low-frequency oscillation analysis.

IV. Eigenvalue and Participation Factor Analysis

In this section, eigenvalue and participation factor analysis is conducted for the simplified model with constant dc voltage assumption. Fig. 11 gives an overall eigenvalue plot for the constant dc voltage model at the marginal condition of $X_g = 1$ pu. The system has 15 eigenvalues with ten complex conjugate eigenvalues denoting five oscillation modes. These ten eigenvalues are noted as λ_i, where $i = 1, \cdots, 10$. Among them, λ_9 and λ_{10} notate the an oscillation mode of 7.4 Hz close to the imaginary axis.

The participation factor table for the constant power model is presented in Table IV. The participation factor table for the constant voltage model is presented in Table V for the five modes. Those two models have very similar participation factor analysis results. In Table V, the leftmost column notates the 15 state variables. Those participation factors with relatively large values are highlighted in bold. Based on the participation factor table, Table VI lists the most relevant factors for the five oscillation modes.

The two high-frequency ($>$ 100 Hz) modes $\lambda_{1,2}$, $\lambda_{3,4}$ are mainly due to grid LC dynamics. Note that VFF influences these two modes. The 58.5 Hz mode $\lambda_{5,6}$ is mainly related to grid dynamics and VFF. The two low-frequency modes $\lambda_{7,8}$ at 7.5 Hz $\lambda_{9,10}$ at 7.8 Hz are influenced by the outer controls and PLL.

Remarks: The participation factor analysis of the dominant oscillation mode at 7.8 Hz indicates that this mode is influenced by the PLL and the VSC outer controls. In

TABLE IV: Participation factor table for the constant dc power model.

State Variable	$\lambda_{1,2}$	$\lambda_{3,4}$	$\lambda_{5,6}$	$\lambda_{7,8}$	$\lambda_{9,10}$
$V_{\rm dc}^2$	0.0002	0.037	0.029	**0.2526**	**0.246**
i_{1d}^g	**0.3633**	0.0752	0.0994	0.0208	0.0035
i_{1q}^g	**0.1343**	0.17	**0.1163**	0.0476	0.0059
i_{gd}^g	0.0471	**0.1446**	**0.2865**	0.0589	0.0146
i_{gq}^g	0.0186	**0.2851**	**0.5107**	**0.1092**	0.0385
$v_{{\rm PCC},d}^g$	**0.3731**	**0.1568**	**0.1199**	0.0293	0.0105
$v_{{\rm PCC},q}^g$	0.1117	**0.3075**	**0.1035**	0.0167	0.0043
θ	0.0117	0.0095	**0.1064**	**0.7867**	**0.3109**
$\Delta\omega$	0.0001	0.0003	0.0066	**0.3591**	**0.1335**
VFF	0.164	0.1187	0.433	0.0912	0.0392
$V_{\rm dc}$ PI	0	0.0043	0.0078	**0.5153**	**0.2217**
$V_{\rm PCC}$ PI	0.0018	0.014	**0.1143**	**0.638**	**0.3596**
q-axis current PI	0.0012	0.0014	0.0182	0.017	0.0118
d-axis current PI	0.0001	0.0012	0.0097	0.0536	0.0086

TABLE V: Participation factor table for the constant dc voltage model

State Variable	$\lambda_{1,2}$	$\lambda_{3,4}$	$\lambda_{5,6}$	$\lambda_{7,8}$	$\lambda_{9,10}$
$V_{\rm dc}^2$	0.0002	0.0391	0.0353	**0.4985**	**0.2519**
i_{1d}^g	**0.3832**	0.0612	0.0968	0.0135	0.0047
i_{1q}^g	**0.1146**	**0.1605**	**0.1207**	0.0481	0.0087
i_{gd}^g	0.0469	**0.1242**	**0.3302**	0.0546	0.0193
i_{gq}^g	0.0161	**0.3067**	**0.4698**	**0.1089**	0.0482
$v_{{\rm PCC},d}^g$	**0.3892**	**0.1344**	**0.1207**	0.0333	0.0134
$v_{{\rm PCC},q}^g$	0.0943	**0.3279**	**0.1049**	0.0195	0.0029
θ	0.0118	0.0100	**0.1061**	**0.5326**	**0.3930**
$\Delta\omega$	0.0001	0.0003	0.0066	**0.1787**	**0.1694**
VFF	**0.1646**	**0.1192**	**0.4271**	**0.1413**	0.0526
$V_{\rm dc}$ PI	0.0000	0.0046	0.0093	**0.4236**	**0.1708**
$V_{\rm PCC}$ PI	0.0018	0.0152	**0.1170**	**0.4449**	**0.4296**
q-axis current PI	0.0012	0.0015	0.0182	0.0205	0.0159
d-axis current PI	0.0000	0.0003	0.0016	**0.4607**	0.0710
$I_{\rm pv}$	0.0001	0.0013	0.0101	0.0420	0.0063

TABLE VI: Constant dc voltage model's eigenvalues and influencing factors

Modes	**Eigenvalue**	**Freq. (Hz)**	**Most relevant factors**
$\lambda_{1,2}$	$-830.2 \pm j2207.4$	351.3	LC dynamics
$\lambda_{3,4}$	$-98.5 \pm j841.0$	133.8	LC dynamics
$\lambda_{5,6}$	$-87.0 \pm j368.1$	58.5	VFF and grid dynamics
$\lambda_{7,8}$	$-73.9 \pm j47.70$	7.5	Outer control and PLL
$\lambda_{9,10}$	$-0.8 \pm j49.2$	7.8	Outer control and PLL

addition, this mode moves to the RHP when the grid becomes weaker. The characteristics of the low-frequency oscillation mode identified using the simplified model indeed matches the existing knowledge on low-frequency oscillations due to VSC in weak grids. To this end, the proposed 15th-order model fulfills the goal of providing both time-domain simulation and small-signal stability analysis for low-frequency oscillations due to weak grid interconnection.

V. Conclusion

In this paper, two state-space models are proposed to represent a grid-connected PV system for low-frequency oscillation analysis. The two models simplify the dc side of the PV system with two different assumptions: constant input power and constant dc voltage. Those two models are compared with an EMT testbed with full details on time-domain simulation results, frequency-domain responses of admittance models, and eigenvalue analysis results. The comparison indicates that the constant voltage model can accurately capture the low-frequency oscillation dynamics at weak grid conditions. Influencing factors of low-frequency oscillations are identified as grid strength, PLL, and inverter's outer controls.

References

[1] NERC, "Integrating inverter-based resources into low short circuit strength systems," December 2017, accessed: 2020-01-21.

[2] S.-H. Huang, J. Schmall, J. Conto, J. Adams, Y. Zhang, and C. Carter, "Voltage control challenges on weak grids with high penetration of wind generation: Ercot experience," in *Power and Energy Society General Meeting, 2012 IEEE*. IEEE, 2012, pp. 1–7.

[3] ERCOT, "Dynamic Stability Assessment of High Penetration of Renewable Generation in the ERCOT Grid," April 2018.

[4] L. Fan and Z. Miao, "An explanation of oscillations due to wind power plants weak grid interconnection," *IEEE Transactions on Sustainable Energy*, vol. 9, no. 1, pp. 488–490, 2018.

[5] L. Fan, "Modeling type-4 wind in weak grids," *IEEE Trans. on Sustainable Energy*, vol. 10, no. 2, pp. 853–864, April 2019.

[6] L. Fan and Z. Miao, "Wind in weak grids: 4 Hz or 30 Hz oscillations?" *IEEE Transactions on Power Systems*, vol. 33, no. 5, pp. 5803–5804, 2018.

[7] Y. Li, L. Fan, and Z. Miao, "Wind in weak grids: Low-frequency oscillations, subsynchronous oscillations, and torsional interactions," *IEEE Transactions on Power Systems*, vol. 35, no. 1, pp. 109–118, 2019.

[8] W. Zhou, Y. Wang, R. E. Torres-Olguin, and Z. Chen, "Effect of reactive power characteristic of offshore wind power plant on low-frequency stability," *Ieee Transactions on Energy Conversion*, vol. 35, no. 2, pp. 837–853, 2020.

[9] First Solar, "Deploying utility-scale PV power plants in weak grids," *2017 IEEE PES General Meeting*, July 2017.

[10] E. I. Batzelis, G. Anagnostou, and B. C. Pal, "A state-space representation of irradiance-driven dynamics in two-stage photovoltaic systems," *IEEE Journal of Photovoltaics*, vol. 8, no. 4, pp. 1119–1124, 2018.

[11] E. Batzelis, G. Anagnostou, I. R. Cole, T. R. Betts, and B. C. Pal, "A state-space dynamic model for photovoltaic systems with full ancillary services support," *IEEE Transactions on Sustainable Energy*, 2018.

[12] N. P. Strachan and D. Jovcic, "Stability of a variable-speed permanent magnet wind generator with weak ac grids," *IEEE Transactions on Power Delivery*, vol. 25, no. 4, pp. 2779–2788, 2010.

[13] Y. Zhou, D. Nguyen, P. Kjaer, and S. Saylors, "Connecting wind power plant with weak grid-challenges and solutions," in *2013 IEEE Power & Energy Society General Meeting*, 2013, pp. 1–7.

[14] Y. Li, L. Fan, and Z. Miao, "Stability control for wind in weak grids," *IEEE Trans. Sustainable Energy*, vol. 10, no. 4, pp. 2094–2103, Oct 2019.

[15] A. Rygg and M. Molinas, "Apparent impedance analysis: A small-signal method for stability analysis of power electronic-based systems," *IEEE Journal of Emerging and Selected Topics in Power Electronics*, vol. 5, no. 4, pp. 1474–1486, 2017.

[16] M. K. Bakhshizadeh, F. Blaabjerg, J. Hjerrild, Ł. Kocewiak, and C. L. Bak, "Improving the impedance-based stability criterion by using the vector fitting method," *IEEE Transactions on Energy Conversion*, vol. 33, no. 4, pp. 1739–1747, 2018.

[17] A. I. Semlyen, "s-domain methodology for assessing the small signal stability of complex systems in nonsinusoidal steady state," *IEEE Transactions on Power Systems*, vol. 14, no. 1, pp. 132–137, Feb 1999.

[18] L. Fan and Z. Miao, "Admittance-based stability analysis: Bode plots, nyquist diagrams or eigenvalue analysis?" *IEEE Transactions on Power Systems*, vol. 35, no. 4, pp. 3312–3315, 2020.

[19] "400-kW Grid-Connected PV Farm (Average Model)," https://www.mathworks.com/help/physmod/sps/examples/400-kw-grid-connected-pv-farm-average-model.html, MATLAB, accessed: 2020-7-20.

[20] M. Sahni, D. Muthumuni, B. Badrzadeh, A. Gole, and A. Kulkarni, "Advanced screening techniques for sub-synchronous interaction in wind farms," in *PES T&D 2012*, 2012, pp. 1–9.

[21] B. Badrzadeh, M. Sahni, Y. Zhou, D. Muthumuni, and A. Gole, "General methodology for analysis of sub-synchronous interaction in wind power plants," *IEEE Transactions on Power Systems*, vol. 28, no. 2, pp. 1858–1869, 2013.

[22] J. Huang, K. A. Corzine, and M. Belkhayat, "Small-signal impedance measurement of power-electronics-based ac power systems using line-to-line current injection," *IEEE Transactions on Power Electronics*, vol. 24, no. 2, pp. 445–455, 2009.

[23] G. Francis, R. Burgos, D. Boroyevich, F. Wang, and K. Karimi, "An algorithm and implementation system for measuring impedance in the dq domain," in *2011 IEEE Energy Conversion Congress and Exposition*, pp. 3221–3228.
[24] P. Van Overschee and B. De Moor, "N4sid: Subspace algorithms for the identification of combined deterministic-stochastic systems," *Automatica*, vol. 30, no. 1, pp. 75–93, 1994.
[25] M. Verhaegen, "Identification of the deterministic part of MIMO state space models given in innovations form from input-output data," *Automatica*, vol. 30, no. 1, pp. 61–74, 1994.
[26] J.-N. Juang and R. S. Pappa, "An eigensystem realization algorithm for modal parameter identification and model reduction," *Journal of guidance, control, and dynamics*, vol. 8, no. 5, pp. 620–627, 1985.
[27] J. Sanchez-Gasca and J. Chow, "Computation of power system low-order models from time domain simulations using a Hankel matrix," *IEEE Transactions on Power Systems*, vol. 12, no. 4, pp. 1461–1467, 1997.
[28] A. Almunif, L. Fan, and Z. Miao, "A tutorial on data-driven eigenvalue identification: Prony analysis, matrix pencil, and eigensystem realization algorithm," *International Transactions on Electrical Energy Systems*, p. e12283, 2019.
[29] P. Kundur, Neal J. Balu, and Mark G. Lauby. Power system stability and control. Vol. 7. New York: McGraw-hill, 1994.
[30] L. Fan, Z. Miao, "A Modular Small-Signal Analysis Framework for Inverter Penetrated Power Grids: Measurement, Assembling, Aggregation, and Stability Assessment," arXiv preprint arXiv:2003.03860, March 2020.
[31] L. Fan and Z. Miao, "Time-Domain Measurements-Based DQ-Frame Admittance Model Identification of Inverter-Based Resources," in *IEEE Transactions on Power Systems*, doi: 10.1109/TPWRS.2020.3040360.
[32] S. Shah and L. Parsa, "Impedance modeling of three-phase voltage source converters in dq, sequence, and phasor domains," *IEEE Transactions on Energy Conversion*, vol. 32, no. 3, pp. 1139–1150, 2017.
[33] A. Yazdani and R. Iravani, *Voltage-sourced converters in power systems: modeling, control, and applications*, John Wiley & Sons, 2010.